Supporting Information

XFCT-MRI Hybrid Multimodal Contrast Agents for Complementary Imaging

Giovanni M. Saladino, Carmen Vogt, Bertha Brodin, Kian Shaker, Nuzhet I. Kilic, Kenth Andersson, Marie Arsenian-Henriksson, Muhammet S. Toprak, Hans M. Hertz

*Corresponding authors. Email: saladino@kth.se, hans.hertz@biox.kth.se

Supporting Text

Magnetization measurements

The magnetization (M) of an ensemble of superparamagnetic nanoparticles is:

$$M = M_S \int_0^{\infty} L(x)\, f(y)\, dy$$

where M_S is the saturation magnetization[41]. L(x) is the Langevin function:

$$L(x) = \coth x - \frac{1}{x}$$

$$x = \frac{M_S' V(y)\, B}{kT}$$

with M_S' being the domain magnetization, V(y) the nanoparticle volume, B the magnetic flux density, k the Boltzmann's constant, and T is the absolute temperature. f(y) is the lognormal size distribution, as follows:

$$f(y) = \frac{1}{y\sigma_M\sqrt{2\pi}} \exp\left[-\frac{\ln^2 y}{2\sigma_M}\right]$$

where $y = D/D_M$. D is the magnetic diameter and D_M its median value[41].

By fitting the magnetization curve as a function of the magnetic field with the given formula[42-43], it is possible to estimate the saturation magnetization, magnetic diameter, and its distribution (M_S, D_M and σ_M).

Sensitivity studies

The contrast to noise ratio (CNR) for both MRI and XFCT was defined as follows:

$$\mathrm{CNR} = \frac{\left|\langle S_{NP}\rangle - \langle S_0\rangle\right|}{\sigma_N}$$

where S_{NP} and S_0 are the pixel intensities within the inner (NP-containing) radius and circular crown (background) of the phantoms, respectively. The average intensities are calculated as the sum of the pixel intensities, divided by the number of pixels. σ_N is the standard deviation of the background signal.

Phantoms with four different NP concentrations were prepared. The MRI signal is proportional to a decaying exponential, as follows:

$$S = k\, e^{-R_2^* \cdot TE}$$

$$S = k\, e^{-\left(r_2^*[Fe] + r_0\right) \cdot TE}$$

$$S = S_0\, e^{-r_2^*[Fe] \cdot TE}, \text{ with } S_0 = k\, e^{-r_0 \cdot TE}$$

with R_2^* as transverse relaxation rate constituted by a solvent-dependent term (r_0) and contrast agent concentration-dependent term (r_2^*). k is a constant term. The CNR for MRI results in:

$$\mathrm{CNR} = \frac{k}{\sigma_N} e^{-r_0 \cdot TE}\left(1 - e^{-r_2^*[Fe] \cdot TE}\right) \propto \left(1 - e^{-r_2^*[Fe] \cdot TE}\right)$$

The XFCT intensity is linearly dependent upon the XRF-active element (Ru) concentration. The offset is given by the background intensity S_0, from the Compton scattering:

$$S_{NP} = S_0 + k\,[Ru]$$

$$\mathrm{CNR} = \frac{k}{\sigma_N}[Ru] \propto [Ru]$$

The CNR is then linear as a function of [Ru]. A decaying exponential and linear fit with a coefficient of determination (R^2) of 98% permitted the estimation of the MRI and XFCT sensitivity, respectively.

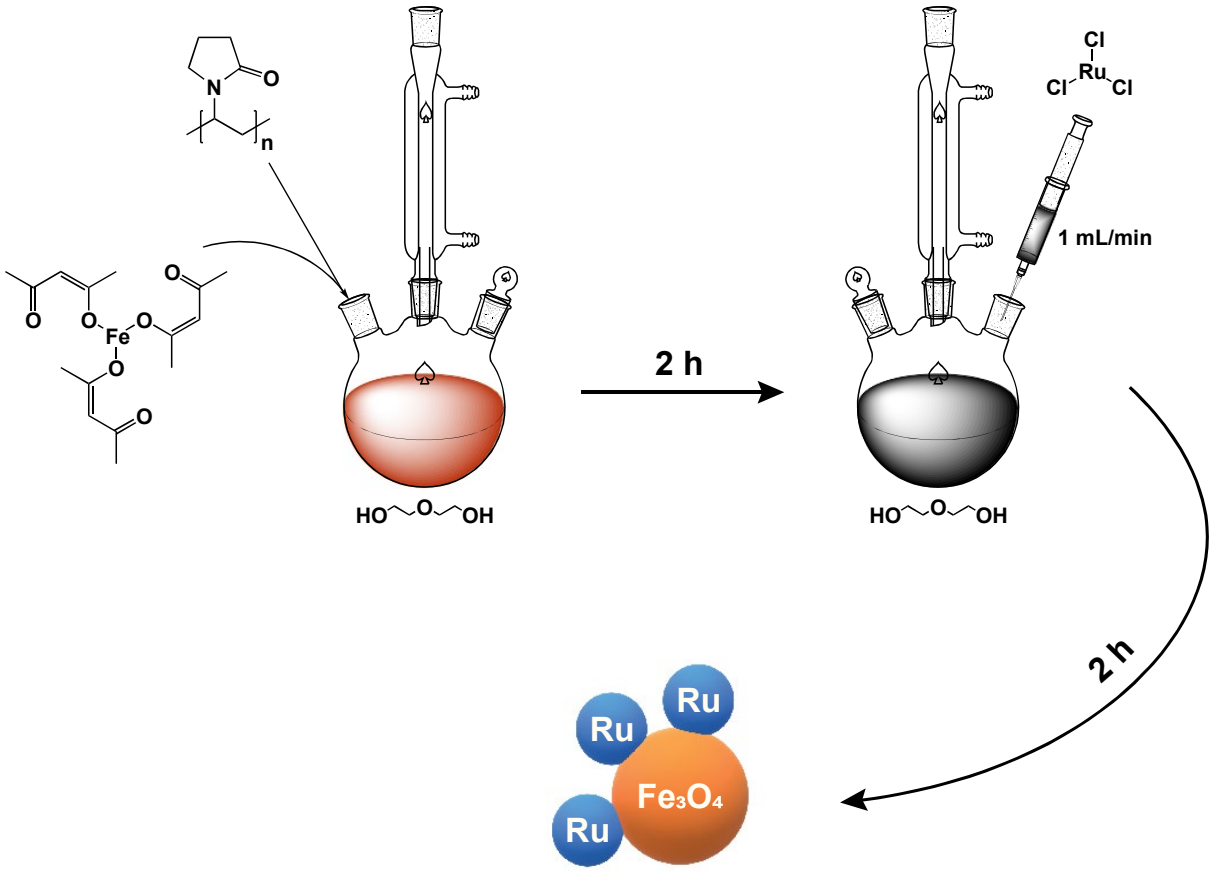

Fig. S1.

Schematic representation of the synthesis conditions. $Fe(acac)_3$ and PVP were dissolved in DEG with magnetic stirring. The solution was kept reacting at the refluxing temperature for 2 h. SPION formation turned the dispersion from dark orange to black. $RuCl_3$ in a water/DEG mixture was injected into the flask (1 mL/min). The dispersion was reacted for other 2 h and cooled down, leading to the formation of Ru-SPIONs.

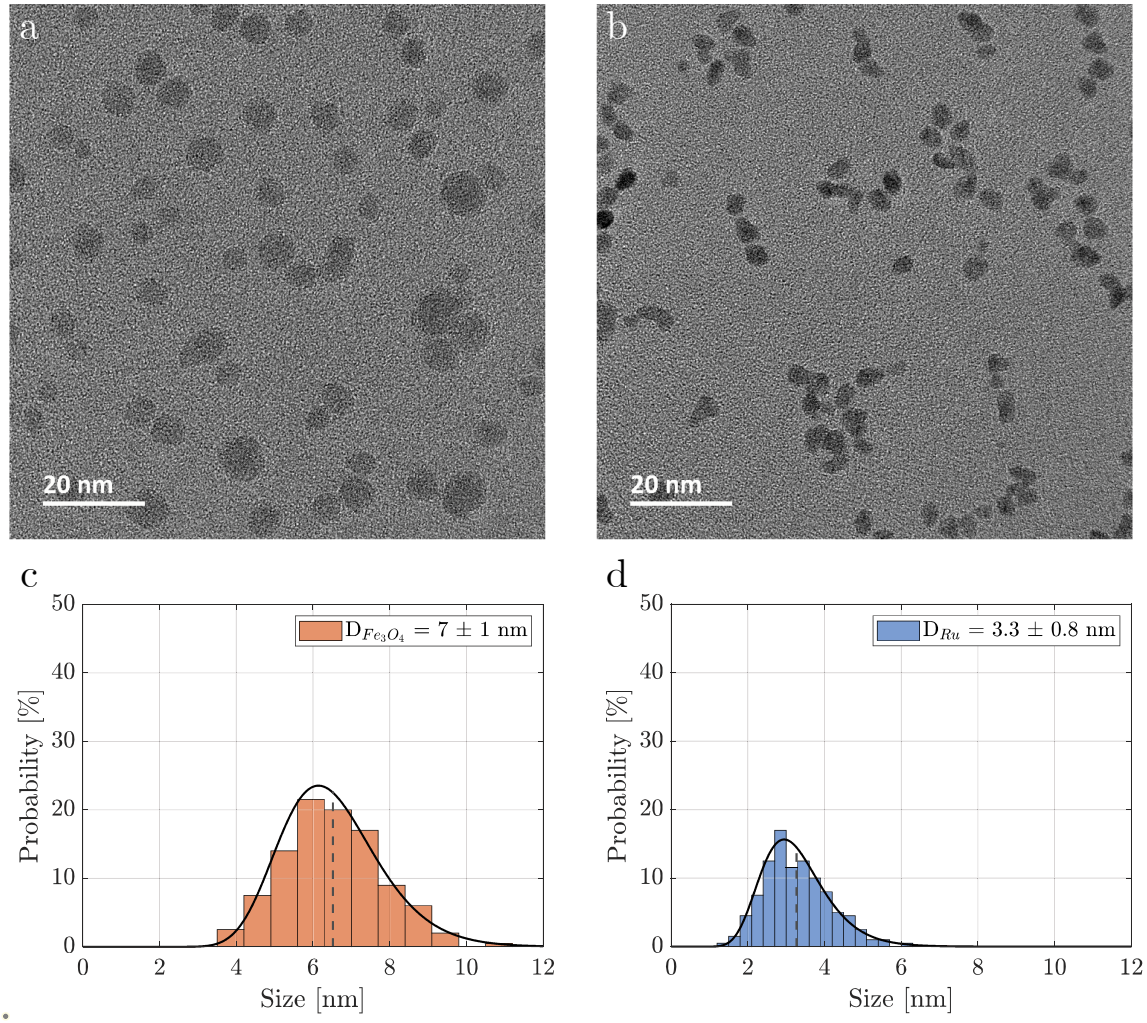

Fig. S2.

SPIONs and Ru NPs. TEM micrographs of SPIONs (**a**) and Ru NPs (**b**) showing the NP morphology. Size distribution histogram, obtained from the TEM micrographs, and lognormal fit (**c**, **d**) with R^2 equal to 98% and 96%, respectively.

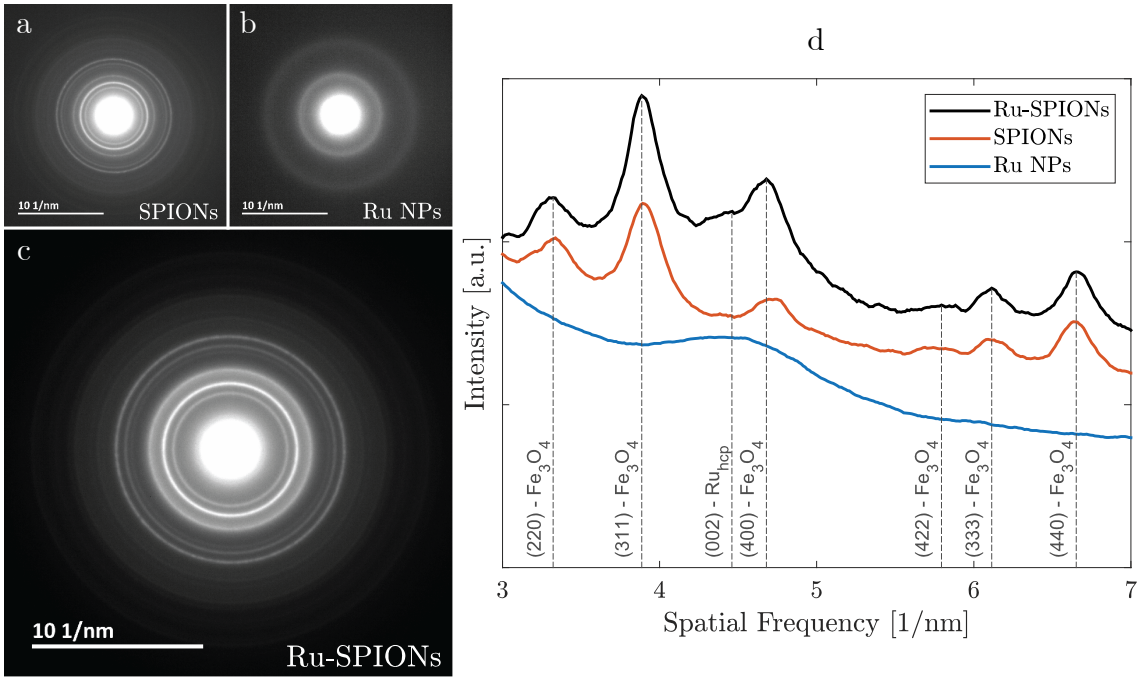

Fig. S3.

Crystal structure analysis with the selected area electron diffraction (SAED) of SPIONs (**a**), Ru NPs (**b**), and Ru-SPIONs (**c**). Linear diffraction profiles (**d**) highlighting the crystal planes of the two NP species. The peaks reveal hcp structure for Ru NPs (COD 9008513) and fcc structure for SPIONs (magnetite/maghemite, CODs 1011032/9006316) in both the bare and hybrid nanostructures.

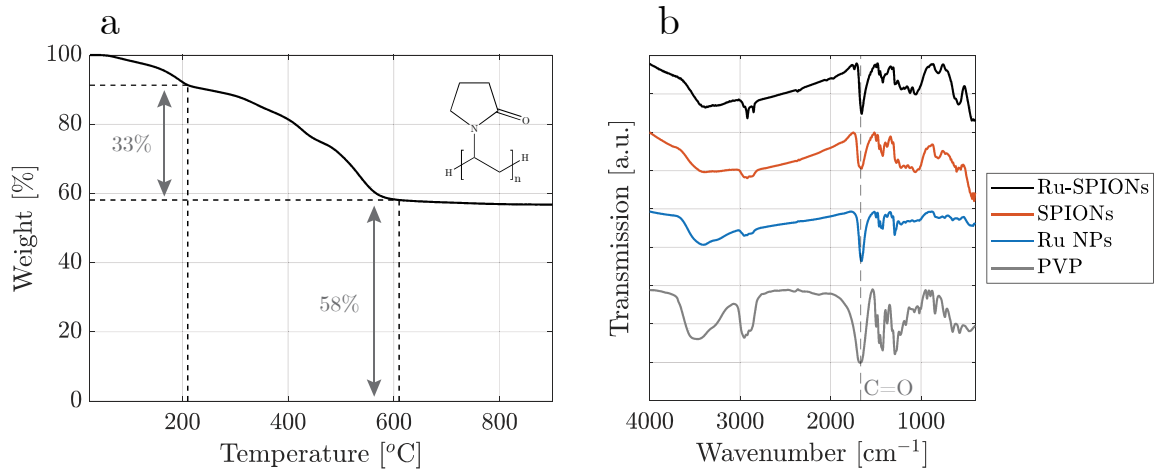

Fig. S4.

TGA thermogram of Ru-SPIONs (**A**), revealing the weight percentage of the organic and inorganic content. Below 200 °C, water desorption is detected. The weight loss between 200 and 600 °C is ascribed to the pyrolysis of PVP on the NP surface. Its molecular structure is schematically shown. FT-IR spectra (**B**) of Ru-SPIONs, SPIONs, Ru NPs and PVP powder are compared, and the main band is associated with the C=O stretching vibration from PVP. A shift between the unbound (1676 cm^{-1}) and bound (1656 ± 1 cm^{-1}) PVP is observed, highlighting the binding and capping mechanisms of PVP on the NP surface.

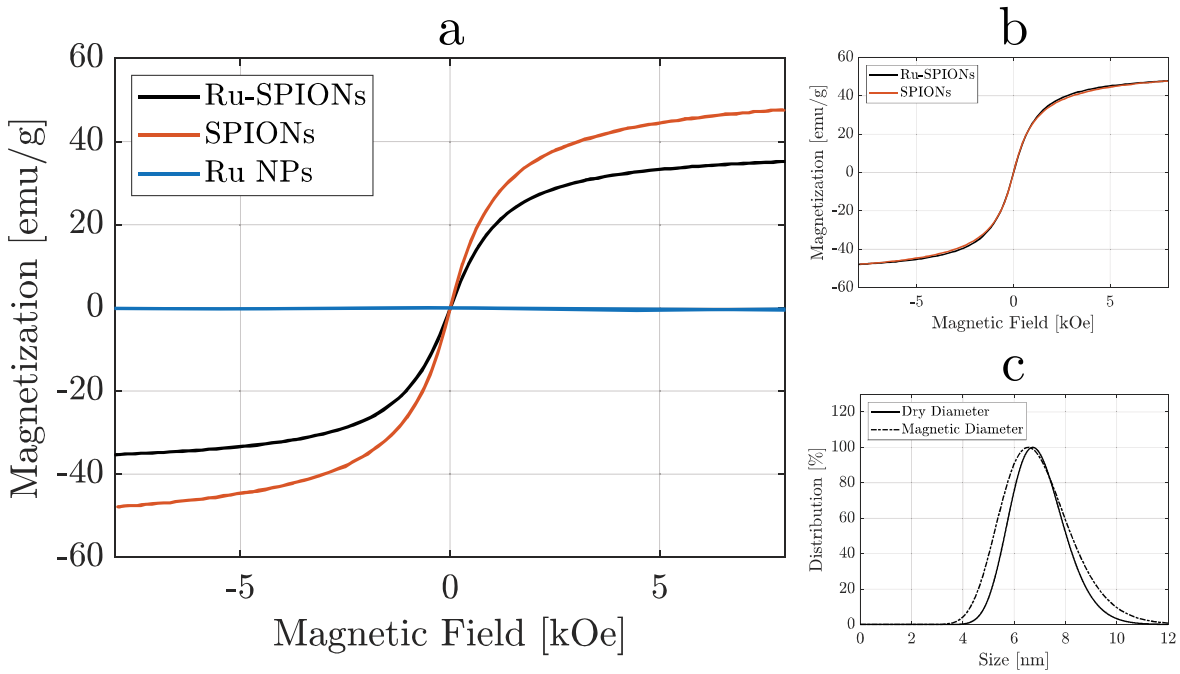

Fig. S5.

Magnetization curve (**a**) obtained by vibrating sample magnetometer (VSM) at 300 K of Ru-SPIONs, SPIONs, and Ru NPs, considering the inorganic content ([Fe_3O_4] + [Ru]). The saturation magnetization was estimated as 38.4 ± 0.2 and 53.2 ± 0.3 emu/g for Ru-SPIONs and SPIONs, respectively. The coercive field (Normalized magnetization curve (**b**) of Ru-SPIONs and SPIONs, weighted only by [Fe_3O_4]. The percentual difference in saturation magnetization per magnetite amount for the two NP kinds, $\Delta[M_{S\,(Ru-SPIONs)}; M_{S\,(SPIONs)})]_{Fe}$, is equal to ≈ 2 %, ascribed to random errors. Comparison of the size distribution functions (**c**) of Ru-SPIONs, obtained from TEM micrograph and magnetic fit, with average diameters of 7 ± 1 and 6.8 ± 1.4 nm (σ_M = 0.2), respectively.

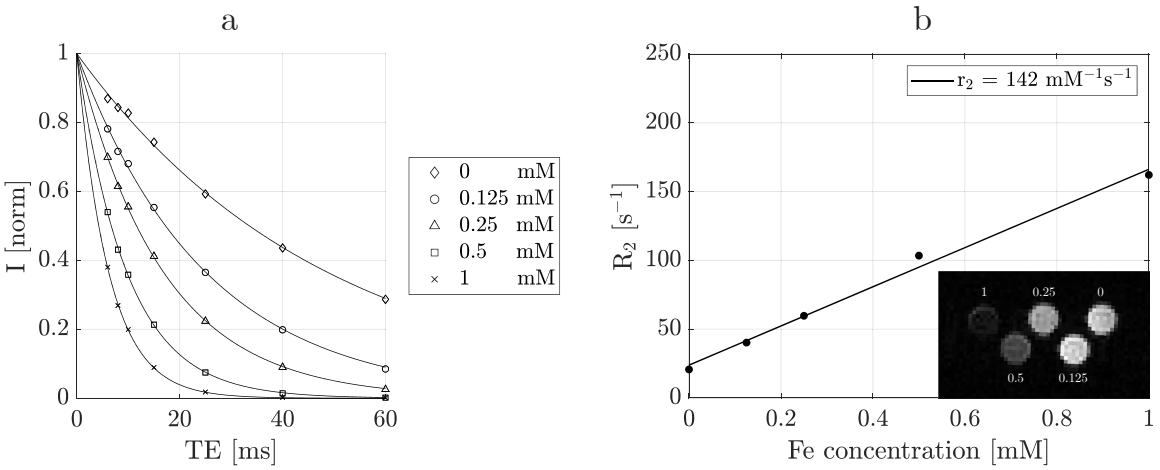

Fig. S6.

T_2 MRI integrated intensity plot (**a**) as a function of the echo time (TE) of phantom syringes with Ru-SPIONs at different iron concentrations in agarose. Transverse relaxivity plot (R_2) as a function of the iron concentration (**b**). The insert shows one slice of the phantom, with TE of 25 ms.

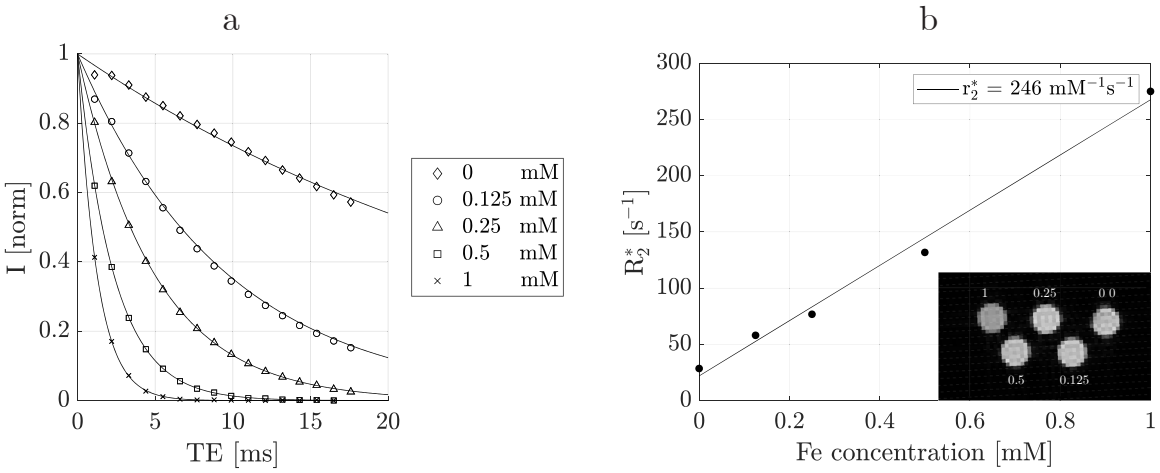

Fig. S7.

T_2^* MRI integrated intensity plot (**a**) as a function of the echo time (TE) of phantom syringes with bare SPIONs at different iron concentrations in agarose. Transverse relaxivity plot (R_2^*) as a function of the iron concentration (**b**). The insert shows one slice of the phantom, with TE of 2.2 ms.

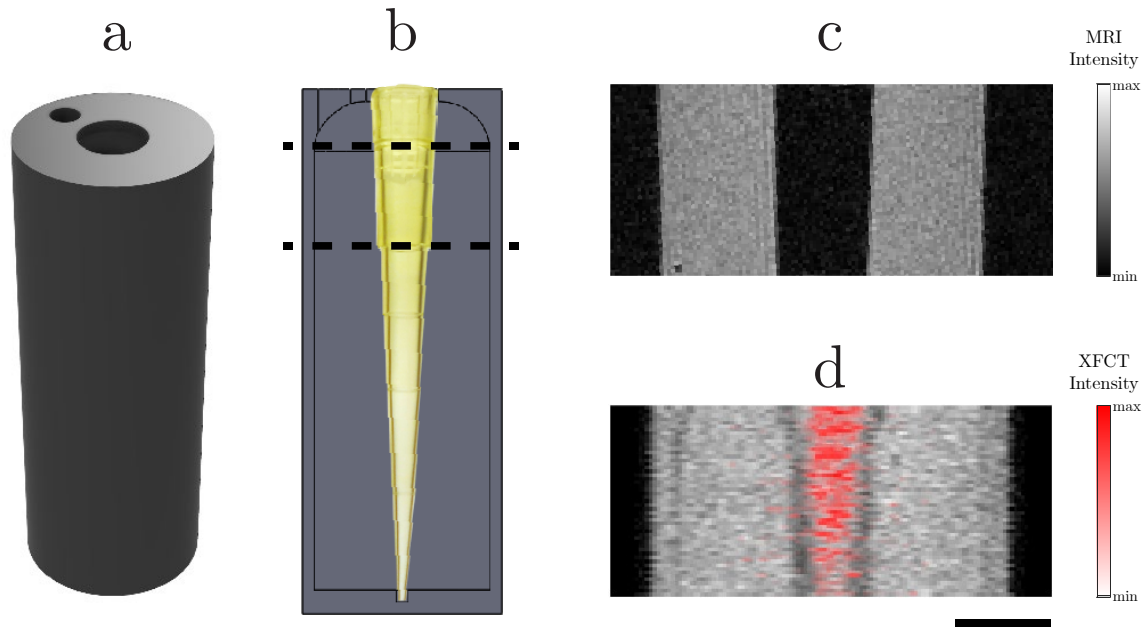

Fig. S8.

3D model (**a**) and schematic cross-section representation (**b**) of the 3D printed phantom for sensitivity studies. The samples are imaged with MRI and XFCT, by scanning 1 cm vertical region (within dashed lines). Representative images of phantom sagittal slices acquired with MRI (**c**) and XFCT (**d**) at 600 µg/mL ([Ru] + [Fe]). Scale bar indicates 5 mm.

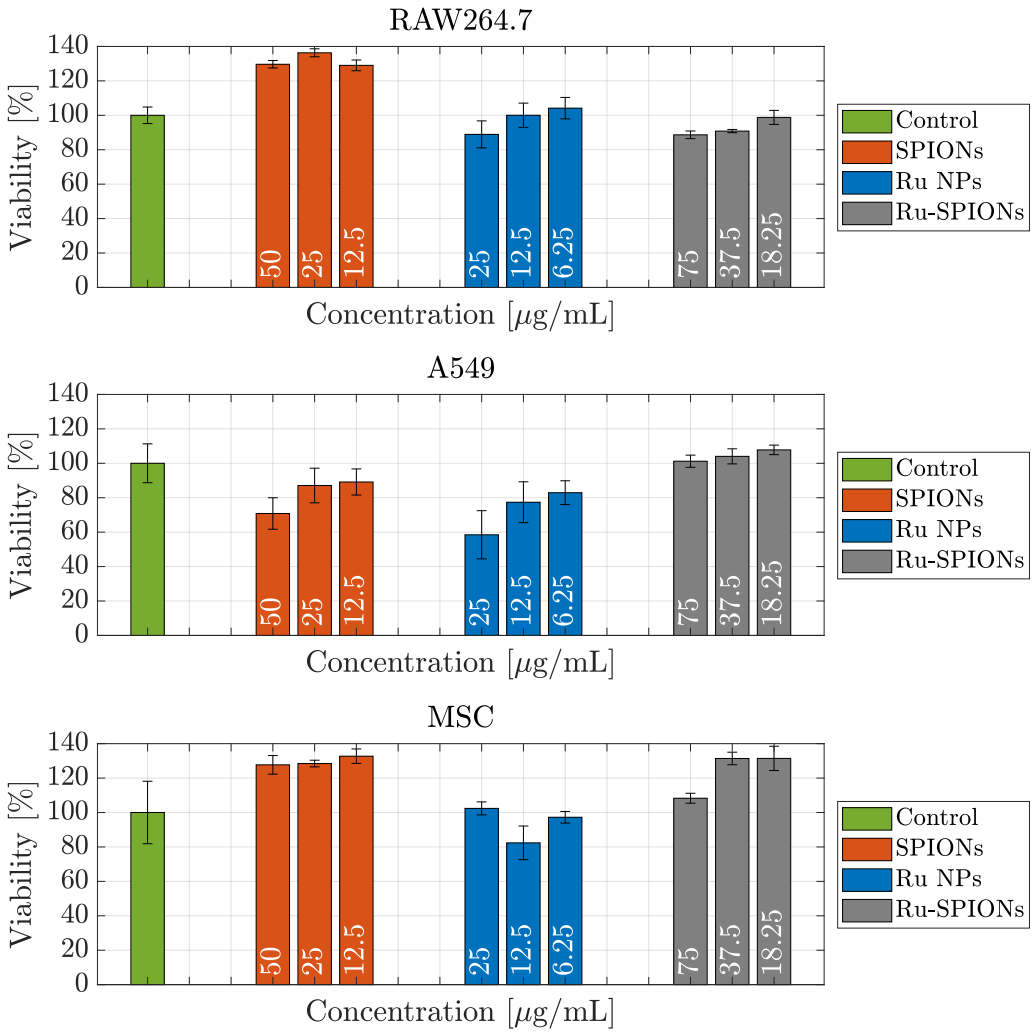

Fig. S9.

CellTiter-Glo® luminescent cell viability (CTG) assay on RAW264.7, A549, and MSC cell lines exposed for 48 h to three concentrations of SPIONs, Ru NPs, and Ru-SPIONs. The fluorescence signal of control (untreated) cells was used for normalization. In the hybrid Ru-SPIONs, the total metallic elemental concentration was kept the same as in the bare NPs ([Ru] + [Fe]), considering the metal ratio [Fe]/[Ru] = 2. Error bars obtained from quadruplicates (± σ).

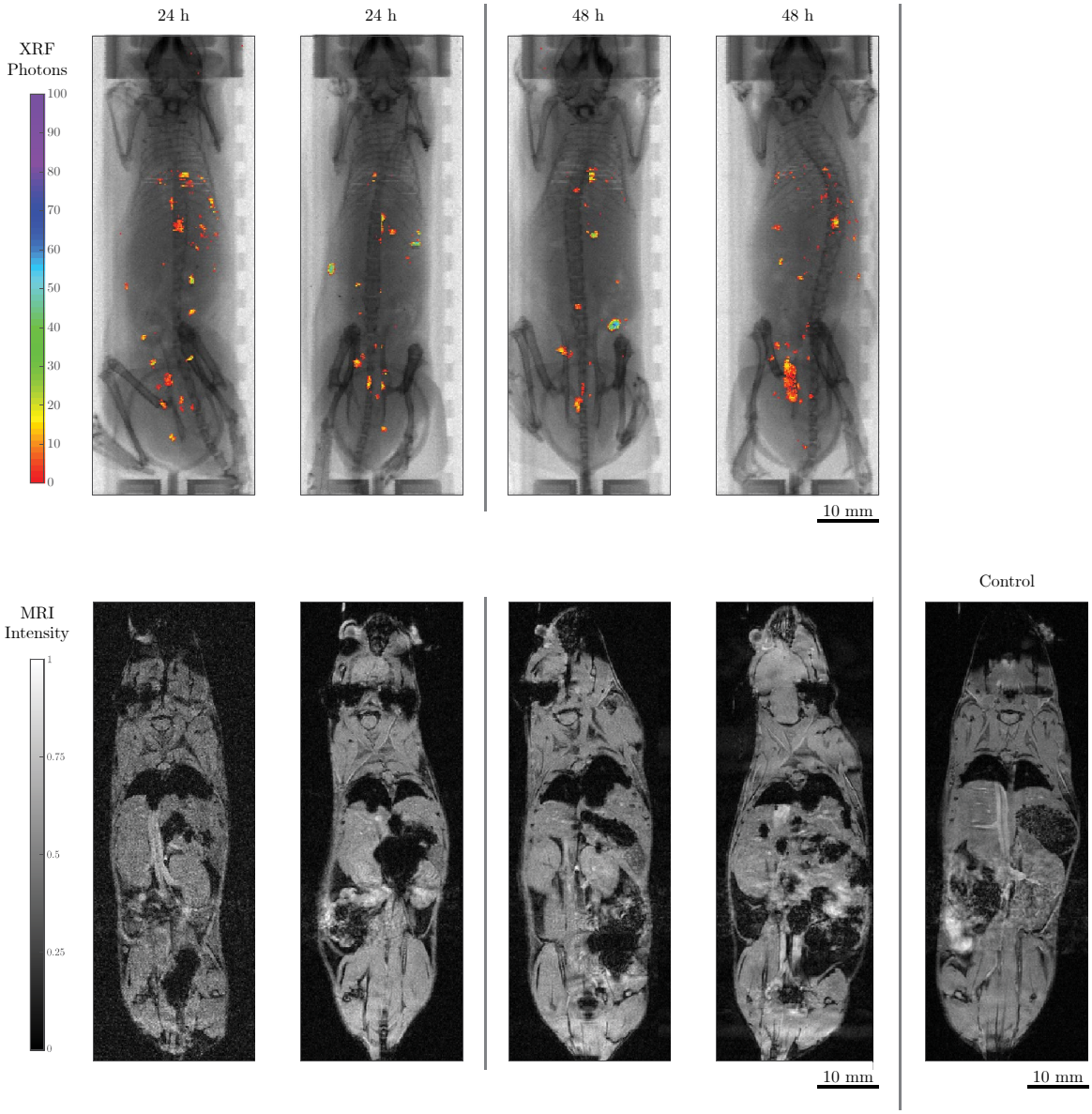

Figure S10.

In vivo XRF-MRI imaging with four different mice injected with Ru-SPIONs *via* an intraperitoneal (IP) injection ([Ru] = 20 mg/kg, [Fe] = 40 mg/kg). Mice were imaged after either 24 h or 48 h, as indicated. The full-body XRF projection images present both the absorption (grey scale) and X-ray fluorescence signal (color scale). One MRI slice was chosen for each mouse, allowing the multi-focal localization of the contrast agents. One mouse without injected NPs was scanned with MRI as the control. Scale bars are 10 mm.

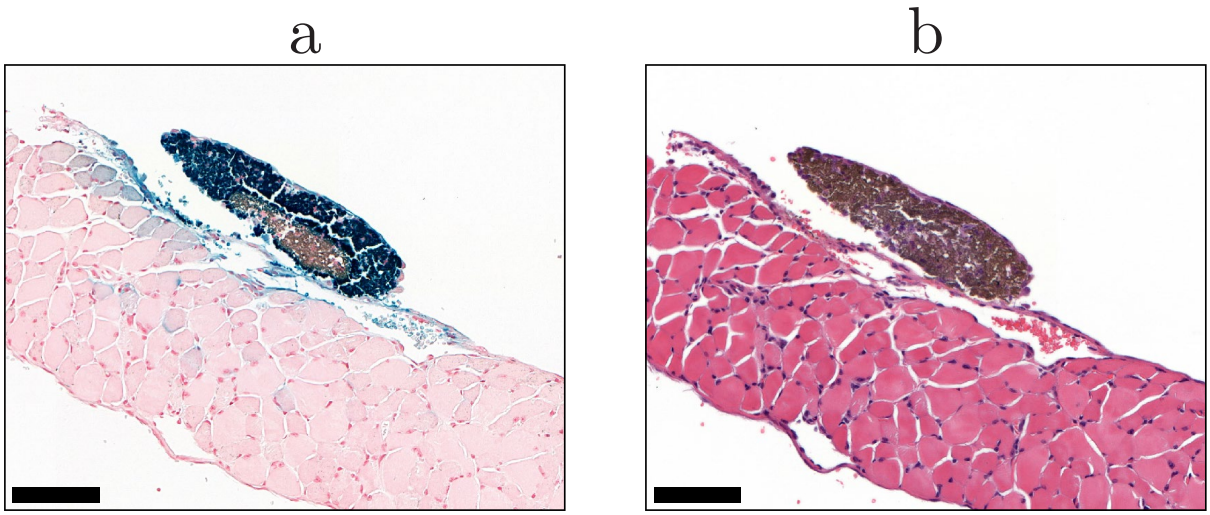

Figure S11.

Diaphragm section of a mouse injected with Ru-SPIONs *via* an intraperitoneal (IP) injection ([Ru] = 20 mg/kg, [Fe] = 40 mg/kg), and sacrificed after 48 h. The sections are stained with Prussian Blue (a) or H&E (b). Scale bars indicate 100 µm.

Movie S1.

Ex vivo full-body XFCT. 3D spatial localization of Ru-SPIONs injected in one mouse imaged after 24 h.

Movie S2.

In vivo local XFCT. Abdominal tomography of one mouse injected with Ru-SPIONs imaged after 48 h for 45 min, under general anesthesia.